A model-based framework for the detection of spiculated masses on mammography[a)]

Mehul P. Sampat
Department of Biomedical Engineering, The University of Texas, Austin, Texas 78712

Alan C. Bovik
Department of Electrical and Computer Engineering, The University of Texas at Austin, Austin, Texas 78712

Gary J. Whitman
Department of Diagnostic Radiology, The University of Texas M. D. Anderson Cancer Center, Houston, Texas 77030

Mia K. Markey[b)]
Department of Biomedical Engineering, The University of Texas, Austin, Texas 78712

(Received 3 September 2007; revised 4 January 2008; accepted for publication 8 February 2008; published 28 April 2008)

The detection of lesions on mammography is a repetitive and fatiguing task. Thus, computer-aided detection systems have been developed to aid radiologists. The detection accuracy of current systems is much higher for clusters of microcalcifications than for spiculated masses. In this article, the authors present a new model-based framework for the detection of spiculated masses. The authors have invented a new class of linear filters, spiculated lesion filters, for the detection of converging lines or spiculations. These filters are highly specific narrowband filters, which are designed to match the expected structures of spiculated masses. As a part of this algorithm, the authors have also invented a novel technique to enhance spicules on mammograms. This entails filtering in the radon domain. They have also developed models to reduce the false positives due to normal linear structures. A key contribution of this work is that the parameters of the detection algorithm are based on measurements of physical properties of spiculated masses. The results of the detection algorithm are presented in the form of free-response receiver operating characteristic curves on images from the Mammographic Image Analysis Society and Digital Database for Screening Mammography databases.
[DOI: 10.1118/1.2890080]

Key words: radon transform, mammography, spiculation and spiculated lesion filters, computer-aided detection, breast cancer, spiculated masses

I. INTRODUCTION

I.A. Clinical significance

The American Cancer Society estimates that 178 480 women will be diagnosed with breast cancer in the U.S. in 2007 (Ref. 1) and 40 460 women will die of the disease. In the U.S., breast cancer is the most common form of cancer among women and is the second leading cause of cancer deaths, after lung cancer.[1] Women in the U.S. have about a 1 in 8 lifetime risk of developing invasive breast cancer.[2,3] Early detection of breast cancer increases the treatment options for patients and also increases the survival rate.

Screening mammography, or x-ray imaging of the breast, is currently the most effective tool for early detection of breast cancer. Screening mammographic examinations are performed on asymptomatic woman to detect early, clinically unsuspected breast cancer. Two views of each breast are recorded: the craniocaudal view, which is a top to bottom view, and the mediolateral oblique (MLO) view, which is a side-view. Radiologists visually search mammograms for specific abnormalities. The most common signs of breast cancer that radiologists look for are clusters of microcalcifications and masses. A mass is a space-occupying lesion seen in at least two different projections.[4] Masses with spiculated margins carry a much higher risk of malignancy than other types of masses or calcifications. Spiculated masses account for about 14% of biopsied lesions, and about 81% of these are malignant.[5]

Early detection via mammography increases breast cancer treatment options and the survival rate.[6] However, mammography is not perfect. Detection of suspicious abnormalities is a repetitive and fatiguing task. For every thousand cases analyzed by a radiologist, only 3–4 cases are malignant and thus an abnormality may be overlooked. As a result, radiologists fail to detect 10%–30% of cancers.[7–9] Approximately two-thirds of these false-negative results are due to missed lesions that are evident retrospectively.[10]

Computer-aided detection (CADe) systems have been developed to aid radiologists in detecting mammographic lesions that may indicate the presence of breast cancer.[11–15]

These systems act as a second reader and the final decision is made by the radiologist. Most studies have shown that CADe systems, when used as an aid, improve radiologists' accuracy in the detection of breast cancer,[16–18] though some studies have found no increase in the number of cancers detected.[19]

Current CADe systems are dramatically better at detecting microcalcifications than masses. The most widely used commercial CADe system is reported to have a 98.5% sensitivity at 0.185 false positives per image (FPI) for microcalcification clusters and a 86% sensitivity at 0.24 FPI for spiculated masses.[18] However, the results vary considerably on different data sets. For example, clinical studies to evaluate the performance of commercial CADe systems for mass detection have reported sensitivities ranging from 67% to 89% with the FPI ranging from 0.40 to 0.74 FPI.[16,17,20–22] For normal images, FP rates of 1.3–1.8 FPI have been reported.[22,23]

I.B. Review of prior work

A number of researchers have focused on the detection of spiculated masses because of their high likelihood of malignancy. The main idea behind previous approaches to the detection of spiculated masses is that since they are characterized by spicules radiating in all directions, one should compute the edge orientations at each pixel. Thus, each pixel is represented by a feature vector, which represents the strongest edge orientation at the pixel. The edge orientation can be computed in a variety of different ways.

Kegelmeyer *et al.*[24] developed a method to detect spiculated masses using a set of five features for each pixel. They used the standard deviation of a local edge orientation histogram (ALOE) and the output of four spatial filters, which are a subset of Law's texture features. The idea of using the ALOE feature is that, as a normal mammogram exhibits a tissue structure that radiates in a particular orientation (from the nipple to the chest), it would have edge orientations primarily in that direction. While in regions containing spiculated lesions, edges would exist in many different orientations. To detect these differences, Kegelmeyer *et al.*[24] computed the edge orientations in a window around each pixel and then generated a histogram of the edge orientations.

Karssemeijer *et al.*[25] detected spiculated masses by a statistical analysis of a map of pixel orientations. The orientation at each pixel was computed from the response of three filter kernels, which are second-order, directional derivatives of a Gaussian kernel in three directions $(0, \pi/3, 2\pi/3)$. These filters form a nonorthogonal basis. They used the relation that at a particular scale, the output at any orientation can be expressed as a weighted sum of the responses of the filters. This was used to determine the orientation at each pixel, and two features for each pixel were derived by a statistical analysis of these pixel orientation maps. The pixels were then classified as suspicious or normal.

Liu and Delp[26] noted that, in general, it is difficult to estimate the size of the neighborhood that should be used to compute the local features of spiculated masses. Small masses may be missed if the neighborhood is too large and parts of large masses may be missed if the neighborhood is too small. To address this problem they developed a multiresolution algorithm for the detection of spiculated masses.[26] A multiresolution representation of a mammogram using the discrete wavelet transform was generated and four features at each resolution for each pixel were extracted. Pixels were then classified using a binary classification tree.

Zhang *et al.*[27] noted that the presence of spiculated lesions led to changes in the local mammographic texture. They proposed that such a change could be detected in the Hough domain, which is computed using the Hough transform. They partitioned an image into overlapping regions-of-interest (ROIs) and computed the Hough transform for each ROI. The Hough domain of each ROI was thresholded to detect local changes in the mammographic texture and to determine the presence or the absence of a spiculated mass.

Zwiggelaar *et al.*[28] proposed a model-based approach for the detection of spiculated masses. They described a technique to characterize patterns of linear structures using principal component analysis and factor analysis. They created statistical models of spiculations created using regions-of-interest containing spiculated masses.

I.C. Overview of this article

In this article, we present a new model-based framework for the detection of spiculated masses. Toward this goal, we have invented a new class of filters called spiculated lesion filters (SLFs) to detect the spatial location where spicules converge. We have also invented a new radon-domain technique for enhancing spicules in mammograms. The enhancement is achieved by computing the radon transform of the image and filtering in the radon domain.

There is a lack of data on physical properties of spiculated masses and we have previously conducted a measurement study in which radiologists measured the physical properties of spiculated masses. As a part of this study we have shown that the physical properties of spiculated masses can be measured reliably.[29] The parameters of the models are based on the spicule widths and lengths, diameter of the central mass, and the number of spicules obtained from the measurement study.

Finally, we have also developed models to reduce the false positives due to normal linear structures (e.g., blood vessels). This is accomplished by using oriented difference-of-Gaussian filters to identify and create a likelihood map of potential normal structures.

II. MATERIALS AND METHODS

II.A. Overview of detection algorithm

The detection algorithm consists of three main components, which are implemented in parallel (Fig. 1). These components are:

(a) spiculation filtering to enhance spicules and detect the spatial locations where spicules converge,

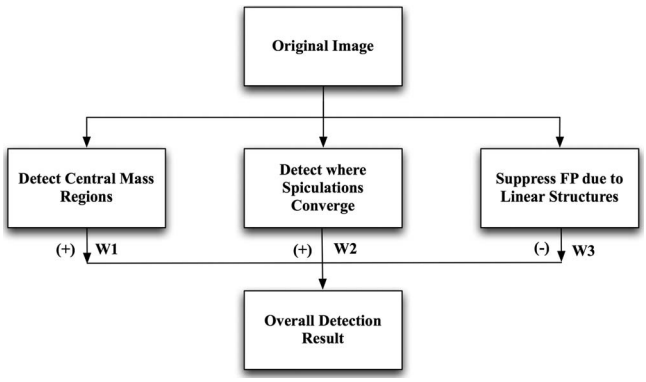

FIG. 1. This figure shows the block diagram of the detection algorithm. This algorithm consists of three components. The first component aims to detect the spatial locations where spicules converge. The second component is designed to detect the central mass regions of the spiculated masses, whereas the third component aims to reduce false positives due to normal linear structures.

(b) detection of the central mass region of the spiculated masses, and
(c) suppression of false positives due to normal linear structures in the parenchyma.

II.A.1. Overview of spiculation filtering

A new algorithm for enhancing spicules is applied followed by filtering with a new class of filters called spiculated lesion filters which are designed to detect patterns of converging linear structures.

II.A.1.a. Enhancement of spiculations The most prominent feature of spiculated masses is the presence of spicules radiating in all directions. We enhance spicules, approximated as curvi-linear structures, by filtering in the radon domain. The radon transform $g(\rho,\theta)$ of a continuous function $f(x,y)$ is defined as[30]

$$g(\rho,\theta)=\int_{y=-\infty}^{y=+\infty}\int_{x=-\infty}^{x=+\infty} f(x,y)\,\delta(\rho-x\cos(\theta)-y\sin(\theta))\cdot dx\cdot dy, \tag{1}$$

where $\delta(r)$ is the Dirac delta function[31] and ρ and θ are parameters of the radon domain. Thus, for any given line in an image, ρ is the length of a perpendicular line segment from the origin to the line and θ is the orientation of the line segment with respect to the x axis. The term $\delta(\rho-x\cos(\theta)-y\sin(\theta))$ in Eq. (1) computes the integral of $f(x,y)$ along the line $\rho=x\cdot\cos(\theta)+y\cdot\sin(\theta)$ and thus the value of $g(\rho,\theta)$ for any (ρ,θ) is the integrated density of $f(x,y)$ along this line. Thus, a line in the image space $f(x,y)$ produces or maps to a point in the radon domain. Also note that lines of different thickness will have different representations in the radon domain. For example, a single pixel thick line would be represented by a point in the radon domain, whereas a 4 pixel thick line would be represented by four points along a column in the radon domain. Thus, by enhancing sharp changes or "local peaks" along the columns in the radon domain, it is possible to detect the corresponding lines in the image by applying a peak detection algorithm.

For our application, the filter $[-1.25,-1.25,1,1,1,1,1,-1.25,-1.25]^T$ was used to detect peaks along the columns in the radon domain. This particular filter was chosen based on the thickness of the spicules obtained from our preliminary measurement studies. Note that, as the sum of coefficients of the filter is zero, the response of this filter to an area of constant or slowly varying values will be zero or very small. After filtering in the radon domain, the inverse radon transform is computed using the filtered backprojection algorithm[32] to obtain an image in which linear structures have been enhanced

$$f(x,y)=\int_0^{\pi} Q_\theta(x\cdot\cos(\theta)+y\cdot\sin(\theta))\,d\theta, \tag{2}$$

$$Q_\theta(t)=\int_{-\infty}^{\infty} S_\theta(w)|w|\exp^{j\cdot 2\pi wt}dw. \tag{3}$$

The enhanced image $f(x,y)$ is obtained using Eq. (2), where $Q_\theta(t)$ is defined in Eq. (3) and $S_\theta(w)$ is the one-dimensional Fourier transform of $g_\theta(r)$.[32] Thus, the output of the enhancement stage is a line-enhanced image and all subsequent processing is performed on this image. Figure 2 shows the various steps of the enhancement algorithm and examples of the results of the enhancement algorithm are shown in Figs. 2(c), 2(e), and 3(b).

The most common approach to computing a discrete radon transform is based on calculating the projection of the image intensities along radial lines oriented at specific angles. Recently, the fast slant stack (FSS) method[33] was developed to compute a discrete form of the radon transform of an image. In previous work, we conducted an observer study and compared the effect of using the traditional approach to discretizing the radon transform versus the new FSS algorithm in our spicule enhancement strategy.[34] We found that observers preferred the images enhanced with the FSS approach and thus we have used this technique to discretize the radon tranform in this study.

II.A.1.b. Detection using spiculated lesion filters We have invented a new class of filters, spiculated lesion filters, to detect the spatial locations where spiculations converge.[35,36] The fundamental idea is to design a "matched filter" for a spiculated lesion. The basic building blocks of the SLF are spiculation filters, which are a new class of complex quadrature filters.

The spiculation filter consists of quadrature components which are the so-called cosine $(f_c(r,\theta;r_0,\sigma,\omega))$ and sine $(f_s(r,\theta;r_0,\sigma,\omega))$ spiculation filters. These components are shown in Figs. 4(a) and 4(b) and are defined as follows:

$$f_c(r,\theta;r_0,\sigma,\omega)=g(r;r_0,\sigma)\cos(\omega\theta), \tag{4}$$

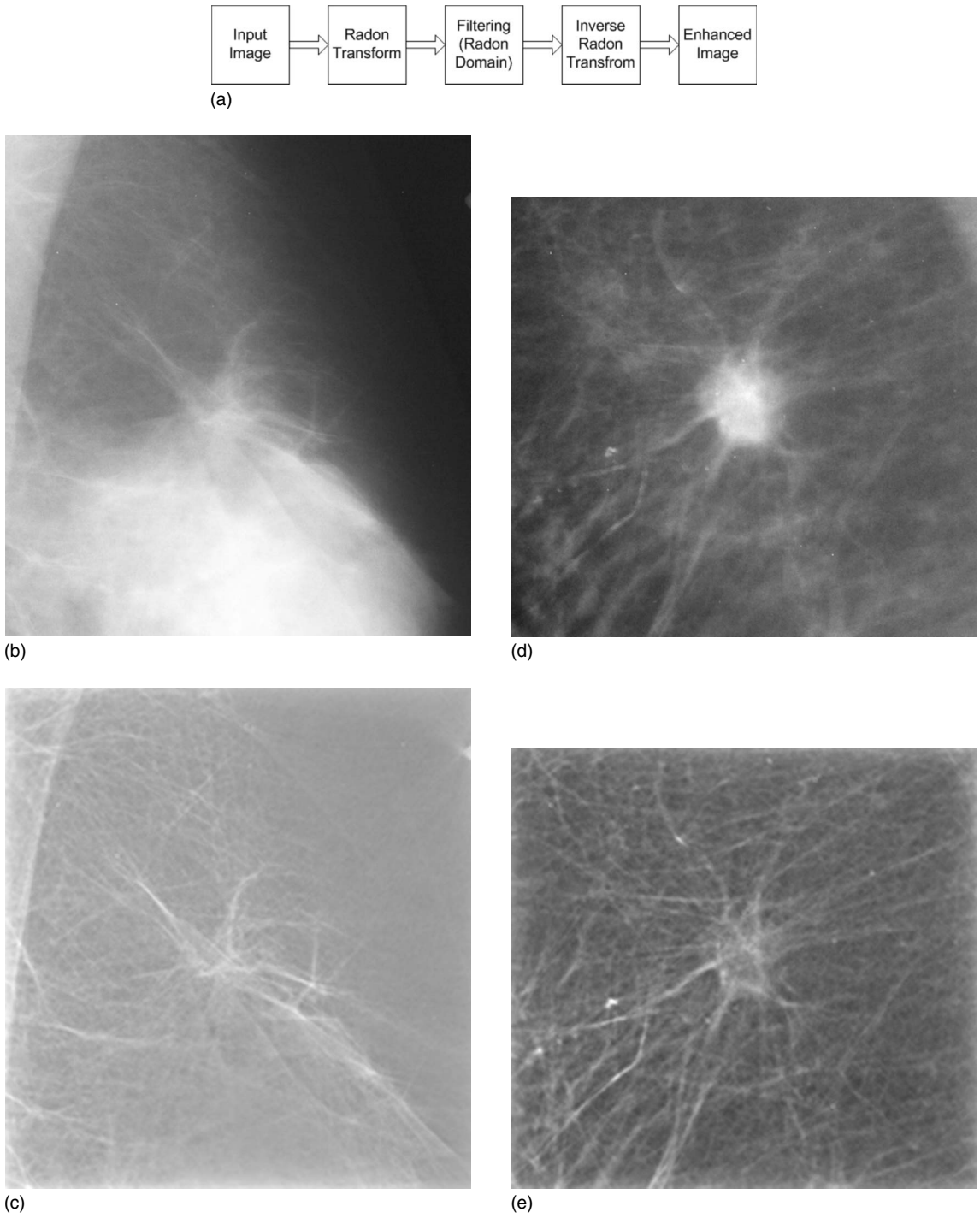

FIG. 2. (a) Flow chart of the spicule enhancement algorithm: First, the radon transform of an image is computed. The radon domain is then filtered with a column filter. Finally, the enhanced image is obtained by computing the inverse radon transform. (b) and (d) show two regions of interest containing spiculated masses and (c) and (e) show the results of the enhancement algorithm, respectively,

$$f_s(r,\theta;r_0,\sigma,\omega) = g(r;r_0,\sigma)\sin(\omega\theta), \tag{5}$$

$$g(r;r_0,\sigma) = \exp((r-r_0)^2/2\sigma^2), \tag{6}$$

where $r=\sqrt{x^2+y^2}$, $\theta=\tan^{-1}(y/x)$, and σ is the standard deviation in pixels.

The parameter r_0 is a size parameter measured in pixels and ω is the modulation frequency measured in cycles per circumference. The Gaussian torus is defined by Eq. (6). The spiculation filters can also be written in the overall phasor form as follows: $h(r,\theta;r_0,\sigma,\omega)=f_c(r,\theta;r_0,\sigma,\omega)+jf_s(r,\theta;r_0,\sigma,\omega)$. Also note that the root-mean-square value $\sqrt{f_c^2+f_s^2}$ of the quadrature components is equal to the toroidal Gaussian envelope function $g(r;r_0,\sigma)$. The complex spiculation filter has the advantage that the sum of the squared

(a)

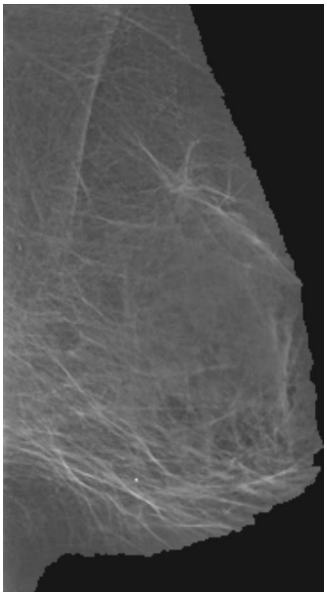

(b)

FIG. 3. A spiculated lesion on a mammogram (circled). (a) Depicts the original image and (b) shows the image obtained after applying the enhancement algorithm. Note that small subtle spiculations are also enhanced and that Fig. 2(b) was a region of interest selected from Fig. 3(a). Other examples of the results of the enhancement algorithm can be found in Figs. 8(b), 9(b), and 10(b).

responses of the two quadrature components is phase independent. Thus, the filter will have the same response to a spiculation even if it has been rotated.

The response of a spiculation filter to a spiculated lesion is important, but it supplies incomplete information regarding the pattern as only a band of a given radius is analyzed. However, by combining multiple spiculation filters to form a SLF, overall spiculated lesion responses may be obtained [examples in Figs. 4(d) and 4(e)]. The SLF can be made to match the size of the central mass region of a spiculated mass by appropriate selection of the inner filter radius. Likewise, spicule length can be matched to the SLF by appropriate selection of the inner and the outer filter radii, the difference between these corresponding to spicule length. Of course, the physical parameters of a particular lesion cannot be known beforehand, and hence, a single appropriate SLF cannot be predetermined. We use measurement data (Sec. II D) to support the selection of the inner and outer radii r_{inner} and r_{outer} for each SLF, as well as the frequency ω of each SLF. The filters are chosen such that the component toroidal Gaussian envelopes intersect at their half-peak values, a strategy that ensures that there will be no gaps in the responses along the radial directions. This approach has been shown to be efficacious in numerous studies involving Gabor filter applications.[37–39] If the radius of a single spiculation filter is r_1 and the toroidal component of that filter is given by $g(r;r_1,\sigma)$, then r_2, the radius of the next spiculation filter in the SLF, is $r_2=r_1+2.3548\cdot\sigma$. Figure 5(a) shows the toroidal components of two spiculation filters of a SLF and Fig. 5(b) shows a cross section through these components.

The normalized cross correlation (NCC) was used for filtering the enhanced image with each SLF. Let T be a SLF of size M-by-M pixels and let I be the image of size L -by-L such that $M \ll L$. The NCC is defined as follows:

$$\text{NCC}(i,j) = \frac{1}{\sigma_T \cdot \sigma_I} \sum_{k=1}^{M} \sum_{m=1}^{M} \{(T(k,m) - \mu_T) \cdot (I(i+k-1, j+m-1) - \mu_I(i,j))\},$$

$$\sigma_T = \sqrt{\sum_{k=1}^{M} \sum_{m=1}^{M} (T(k,m) - \mu_T)^2}$$

$$\sigma_I = \sqrt{\sum_{k=1}^{M} \sum_{m=1}^{M} (I(i+k-1, j+m-1) - \mu_I(i,j))^2}, \quad (7)$$

where μ_T is the mean of the template and $\mu_T(i,j)$ is the mean of the subimage centered at (i,j). Let $\text{OP}_{\cos}$ and $\text{OP}_{\sin}$ be the outputs obtained after filtering the enhanced image with the two quadrature components of the SLF (cosine and sine SLFs). The magnitude response OP_{mag} and the phase response OP_{phase} of the SLF are defined as

$$\text{OP}_{\text{mag}} = \sqrt{(\text{OP}_{\cos})^2 + (\text{OP}_{\sin})^2}, \quad (8)$$

$$\text{OP}_{\text{phase}} = \arctan(\text{OP}_{\sin}/\text{OP}_{\cos}). \quad (9)$$

The magnitude response OP_{mag} of the SLF is smoothed with a Gaussian filter (sigma=2). This post-filtering has been shown to be beneficial in numerous studies involving Gabor filter applications.[37–39] If the SLF "matches" a spiculated lesion, a peak would be obtained at the spatial location corresponding to the center of the spiculated lesion. Thus, suspicious regions can be identified by detecting the local peaks in the overall output. Note that the larger the overall output at a particular spatial location, the higher the likelihood that the spatial location corresponds to the center of a spiculated le-

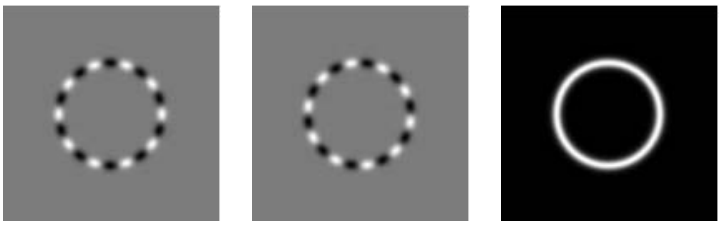

(a) Cosine Spiculation Filter with $\sigma = 2,\ \omega = 10$

(b) Sine Spiculation Filter with $\sigma = 2,\ \omega = 10$

(c) Gaussian torus with $\sigma = 2$

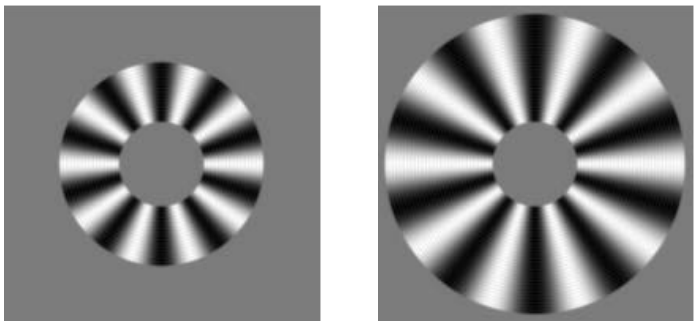

(d) Spiculated Lesion Filter $\sigma = 1,\ \omega = 10$

(e) Spiculated Lesion Filter $\sigma = 1,\ \omega = 10$

FIG. 4. Example of a spiculation filter and SLFs: (a) and (b) show the two quadrature components of the spiculation filter, namely, the cosine and sine spiculation filters, respectively. The toroidal Gaussian envelope of the spiculation filter is shown in (c). In (d) and (e), two spiculated lesion filters, each composed of spiculation filters of progressively increasing radii and matching radial frequencies ω are shown. The SLFs in (d) and (e) have the same inner radius but different outer radii. These would correspond to lesions where the central mass is the same size but the spicule lengths differ.

sion. A likelihood map for the locations of spiculated masses, SLF_Maxima, is computed by taking the maximum SLF output across all SLFs,

$$\mathrm{SLF\_Maxima}(x,y) = \max\{\mathrm{SLF}_1(x,y), \mathrm{SLF}_2(x,y), \ldots, \mathrm{SLF}_N(x,y)\}(\forall x,y). \quad (10)$$

II.A.2. Detection of the central mass region of the spiculated masses

Gaussian filters are used to detect the central mass region. While other studies have used Gaussian filters for mass detection, key differences in our approach are that the size of the filters was selected from the measurement data and that a set of 25 Gaussian filters was used. The maximum output value across all Gaussian filters computed at each pixel (Gaussian_Maxima) represents the likelihood of the presence of a mass.

II.A.3. Suppressing false positive due to normal linear structures in the parenchyma

In addition to spicules, structures such as blood vessels, ducts, and other linear elements in the tissue parenchyma can also be enhanced. The spiculated lesion filters can respond to the criss-crossings of these normal structures and thus generate false positives. We used a strategy based on oriented difference-of-Gaussian (DOG) filters to identify and suppress false positives.

At each spatial location the image was filtered with an elongated and oriented DOG filter (Fig. 6). The orientation of this filter was the local orientation ($\theta_{i,j}$) at that spatial location: $\theta_{i,j} = \arctan(Gy/Gx)$, where Gy and Gx are the gradients in the y and x directions, respectively. Since the goal is to identify linear structures that are not spicules, the width of the central lobe is greater than the largest width of the spicules measured.

II.A.4. Summary of the detection algorithm

As both the spiculated lesion filters and the Gaussian filters provide evidence for the presence of a spiculated mass, the outputs from these filters are summed up in the overall detection output. The responses from the oriented DOG filters denote the likelihood of normal structures (e.g., blood vessels) and thus they are subtracted in the overall detection output. Thus,

$$\begin{aligned}\mathrm{Overall\_Output} = {} & W_1 \cdot \mathrm{SLF\_Maxima} \\ & + W_2 \cdot \mathrm{Gaussian\_Maxima} \\ & - W_3 \cdot \mathrm{DOG\_Response},\end{aligned}$$

where W_1, W_2, W_3 are weights that can be applied to the output of each of the components of the detection algorithm. In this study, we weighted the output of the components equally.

II.B. Data description

Three sets of images were used for this study. Two sets of images were obtained from the Digital Database for Screening Mammography[40,41] (DDSM) and one from the Mammographic Image Analysis Society (mini-MIAS).[42,43]

The DDSM is the largest publicly available data set of digitized mammograms and consists of 2620 cases. Each abnormality has been outlined by a radiologist and this was used as the "ground truth" for detection of spatial locations of spiculated lesions. Thus, if the output of the detection algorithm was located within this outline, then it was counted as a true-positive output. Note that as we do not aim

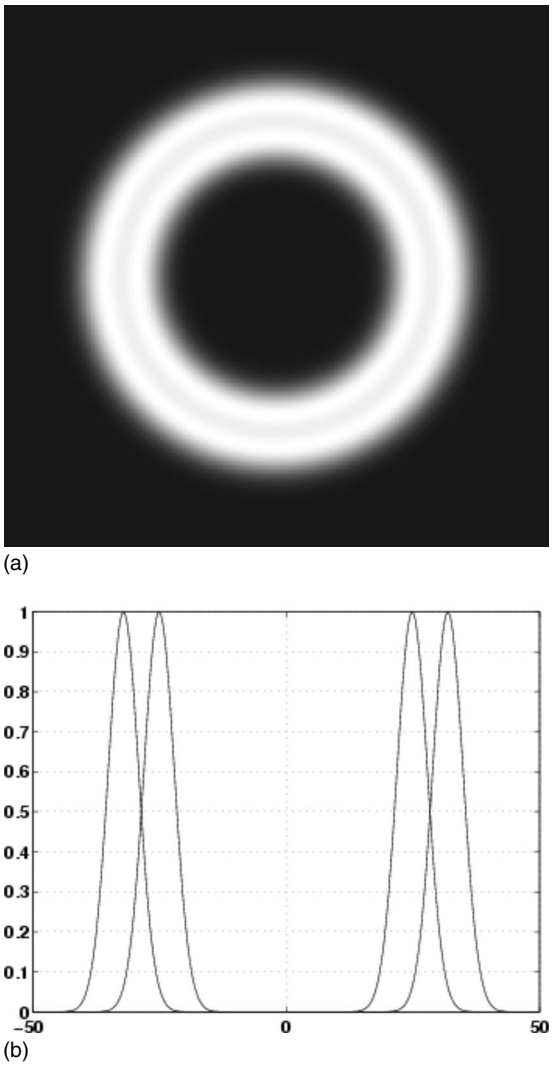

FIG. 5. (a) shows the toroidal components of two spiculation filters of a spiculated lesion filter and (b) shows a cross section through these components. The filters are chosen such that the component toroidal Gaussian envelopes intersect each other at their half-peak values, a strategy that ensures that there will be no gaps in the responses along the radial directions.

to "segment" the mass and thus the "boundary" marked on images in the DDSM database is adequate for assessing our algorithm. The images in the DDSM database were scanned at 50 μm. For computational efficiency, in this study we decimated the images from the DDSM database by a factor of 4 and thus the image resolution was 200 μm.

The images in the mini-MIAS database have a resolution of 200 μm and each image has been clipped or padded so that it is 1024×1024 pixels.[42] The x and y image coordinates of the center of the abnormality and the radius (in pixels) of the circle enclosing the abnormality are provided and the ground truth is created from this data. Thus, if the output of the detection algorithm was located within this circular region, then it was counted as a true-positive output.

II.B.1. Image set 1: Images used for the measurement study

A set of 21 images of spiculated masses from the DDSM database was used for the measurement study (Sec. II D). All

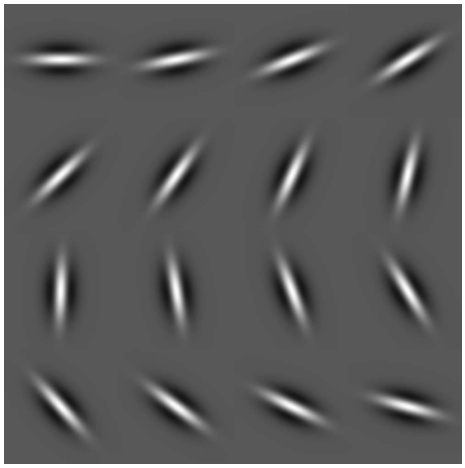

FIG. 6. This figure shows a subset of the elongated and oriented DOG filters used. The output of these filters is used to suppress the FPs due to linear structures such as blood vessels and ducts.

images were MLO view images from a single scanner and a range of image density ratings were represented in this set.[29]

II.B.2. Image set 2: Images from mini-MIAS database used for testing

A set of 50 images from the mini-MIAS database[42] was used to test the detection algorithm. This set consists of all 19 spiculated masses and the first 31 normal images from the mini-MIAS database. These images were scanned with a single digitizer, each contained a single lesion, and all images were MLO view images.

II.B.3. Image set 3: Images from the DDSM database used for testing

A set of 100 images from the DDSM database was used to test the detection algorithm. This set consists of 50 images of spiculated masses and 50 normal images. The selected cases were digitized by a single scanner and represented a range of density ratings, subtlety ratings, and pathology. There was no overlap between the images used in the measurement study and those used to evaluate the detection algorithm. A list of the images used in each of the three sets can be obtained on the authors' website.[44]

II.C. Measurement of physical parameters

We use the ROI manager plugin of NIH ImageJ (Ref. 45) to enable a user, with minimal training, to place markers at specific locations, and compute the Euclidean (pixel) distance between the markers. This interface allows for measurement of spicule width both at the base of the spicule (where it meets the mass) as well as at other points along the spicule. The user can also measure the lesion dimensions of the central region along the principal axes. In addition, the operator can trace the spicule along its entire length using straight lines, to determine spicule length, and the user can count the spicules associated with a lesion. Since the reso-

TABLE I. Average measurements (mm) made by the radiologist (G.J.W.) (± standard deviation) across all spicules, all MLO images for spiculated masses. These measurements represent the average value across 21 spiculated masses.

Major axis	Spicule width	Spicule length	Number of spicules
15.10(±7.98)	1.00(±0.296)	8.80(±2.62)	17.57(±6.01)

lution of the images is known, the pixel measurements can be converted into physically meaningful quantities (e.g., millimeters).

A radiologist (G.J.W.) used NIH ImageJ to measure the length and the width at the base for all spicules from each spiculated mass. He also measured the length of the major axis of the central region of each lesion. The number of spicules that were visible for each lesion were also counted. Table I summarizes the measurements made by the radiologist for the various parameters of spiculated masses. The details of this measurement study can be obtained in the article by Sampat *et al.*[29] In previous work (Sampat *et al.*[29]), we demonstrated that it is feasible to make reliable measurements of the physical properties of spiculated masses on mammography using this system.

II.D. Selection of detection algorithm parameters based on measurement data

The average width of spicules in our measurements was 5 pixels (1 mm). Thus, to enhance spicules, each column of the radon transform of the image is convolved with $[-1.25, -1.25, 1, 1, 1, 1, 1, -1.25, -1.25]^T$.

To account for variability in the shape and the structure of spiculated lesions, SLFs with different parameters are used. The joint probability density function of the three variables (central mass region radius, length of spicules, and the number of spicules) was estimated by the kernel method with Gaussian kernels.[46] The joint estimate was then randomly sampled to select the parameters of the SLFs (Fig. 7) and the Gaussian filters. For the Gaussian filters, the parameter sigma was selected so that the half peak radius was equal to radii measurements obtained after the random sampling of the joint density function (sigma=radius/1.177). Note that while all of the parameters are based on the measurement data, the number of filters was an empirical choice that could be optimized in future studies.

III. RESULTS

In Figs. 8–10 we show the response of each step of the detection algorithm. In Figs. 8(b), 9(b), and 10(b) we demonstrate the effect of the spicule enhancement algorithm and the output after filtering with the spiculated lesion filters is shown in Figs. 8(c), 9(c), and 10(c). The output after filtering with a bank of Gaussian filters is used to detect the central mass region [Figs. 8(d), 9(d), and 10(d)] and the oriented DOG filters [Figs. 8(e), 9(e), and 10(e)] are used to suppress some linear structures.

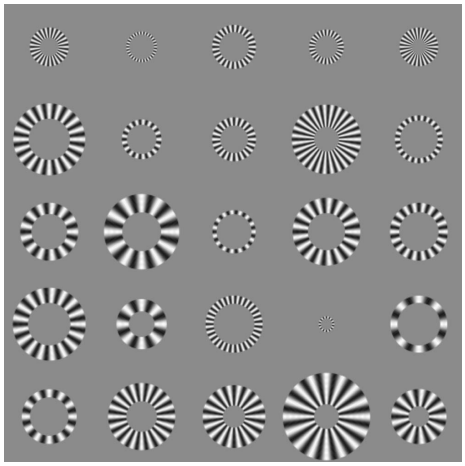

FIG. 7. The set of 25 SLFs used for the detection of spiculated masses. To select the parameters of these SLFs an estimate of the joint pdf of the central mass region radius, length of spicules, and number of spicules was obtained. This joint estimate of the pdf was then randomly sampled to select the parameters of the SLFs.

To report the performance of the detection algorithm, free-response receiver operating characteristic (FROC) curves were generated. A FROC curve is obtained by plotting sensitivity on the y axis and the number of false positives per image on the x axis.

The overall output from the detection algorithm is normalized by subtracting the mean and dividing by the standard deviation. A threshold is applied to the normalized overall output and pixels that have a value greater than the threshold are viewed as potential lesions. A pixel is counted as a true positive if it lies within the ground truth outlined by the radiologist. If multiple pixels within the ground truth are marked, they are all counted as a single true positive. Moreover, a pixel was marked only if the distance between it and any other marked pixel was at least the average radius of the central mass region.

At each threshold of the detection output, the FROC curve provides the sensitivity and FPI. For the images from the MIAS data set we obtained a sensitivity of 84% at 3 FPI (Fig. 11). For a set of 50 images of spiculated masses and 50 normal images from the DDSM, we achieved a sensitivity of 88% at 2.7 FPI (Fig. 12).

Table II summarizes the results of prior studies for the detection of the spiculated masses, though it is not possible to directly compare studies that used different data sets. From Table II we see that the number of spiculated masses used in previous detection studies is quite small. The major disadvantage of testing an algorithm on a small set of images is that the natural variations among the spiculated masses are not seen by the algorithm. To the best of our knowledge our experiments are the largest detection studies (in terms of the number of spiculated masses used).

IV. DISCUSSION AND CONCLUSION

In this article, we have presented a new model-based framework for the detection of spiculated masses. Toward this goal, we have made several novel contributions.

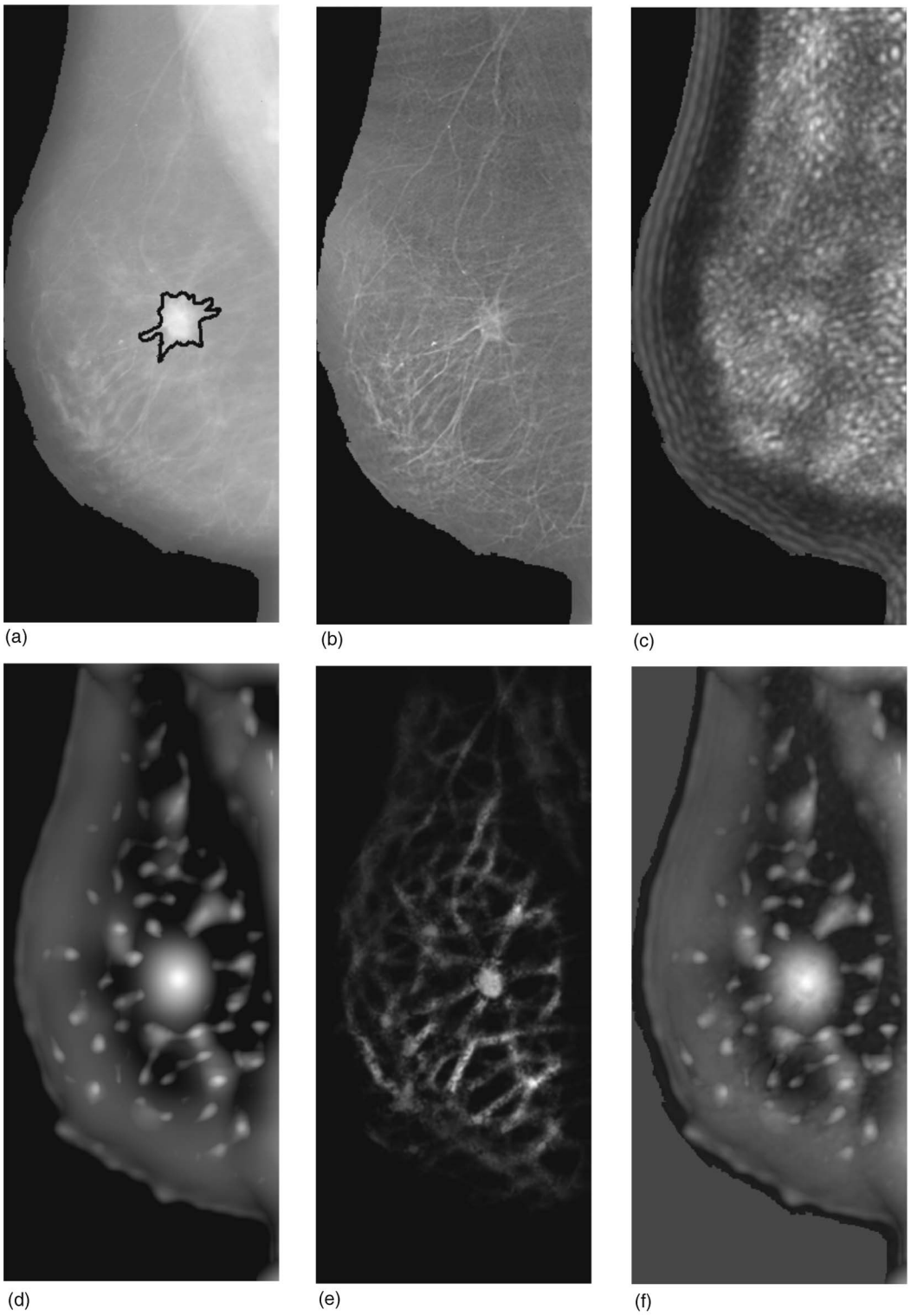

FIG. 8. This figure shows the output obtained at each step of the detection algorithm: (a) Original image and the ground truth outlined by the radiologist. (b) The image obtained from the enhancement algorithm. (c) The output of the spiculated lesion filters (d) The output from the Gaussian filters. (e) The output from oriented DOG filters. (f) The overall output of the detection algorithm.

IV.A. Measurement study

We use measurements of lesion properties to guide the design of the detection algorithm. While other groups have conducted studies to measure physical characteristics of masses on mammography, most have only reported the mass size for mixtures of different types of masses. For example, Varela *et al.* reported the average mass size (from radiologists' annotations) for 99 malignant masses and 98 benign

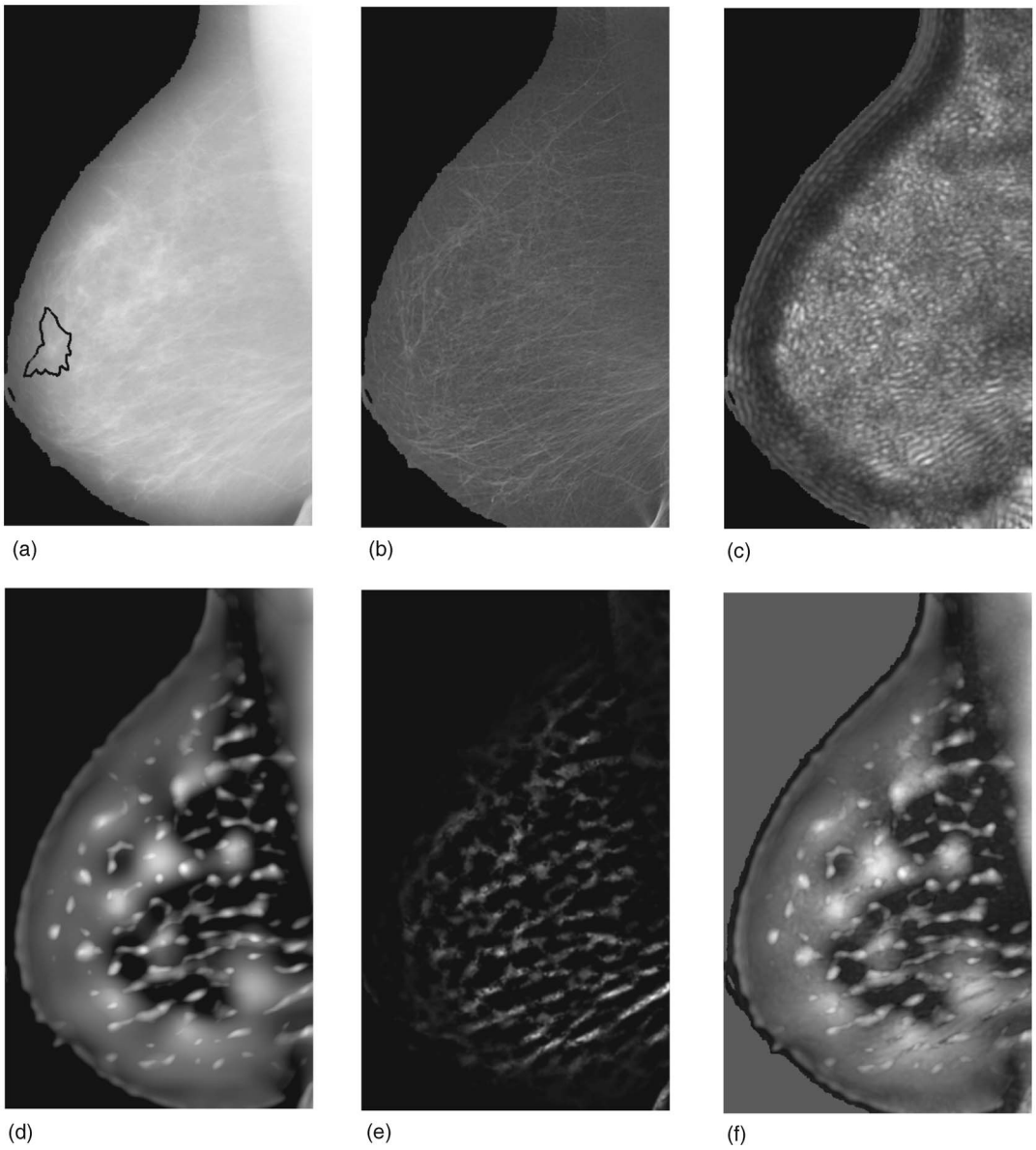

FIG. 9. This figure shows the output obtained at each step of the detection algorithm: (a) Original image and the ground truth outlined by the radiologist. (b) The image obtained from the enhancement algorithm. (c) The output of the spiculated lesion filters. (d) The output from the Gaussian filters. (e) The output from oriented DOG filters. (f) The overall output of the detection algorithm.

masses.[47] However, only the mass sizes for spiculated masses were not reported. Saunders *et al.*[48] measured the physical characteristics of masses and calcifications and these measurements were used to simulate breast masses and calcifications. A total of 152 masses were measured and the average size for malignant and benign masses was reported. To the best of our knowledge, the only study where radiologists annotated spicules and other linear structures was conducted by Zwiggelaar *et al.*,[49] on a set of 15 images. In this study, cross-sectional profiles of linear structures were used to classify these structures as spicules, blood vessels, ducts, etc. In our study all spicules were localized and measured by a radiologist, whereas in the study by Zwiggelaar linear structures were automatically detected and only a random subset was annotated by a radiologist.

IV.B. Spicule enhancement algorithm

We have proposed a new technique for enhancing spicules in mammograms based on filtering in the radon domain. The parameters of the filter are chosen based on the width of spicules obtained from the measurement studies.

The related Hough transform has been applied for the detection of spiculated masses by other researchers.[27] However, a key innovation of our enhancement algorithm is the filtering of the coefficients in the radon domain. To the best of our knowledge, this has not been proposed in CADe or other image processing applications.

IV.C. Spiculated lesion filters

We have invented a new class of filters called spiculated lesion filters to detect the spatial location where spicules con-

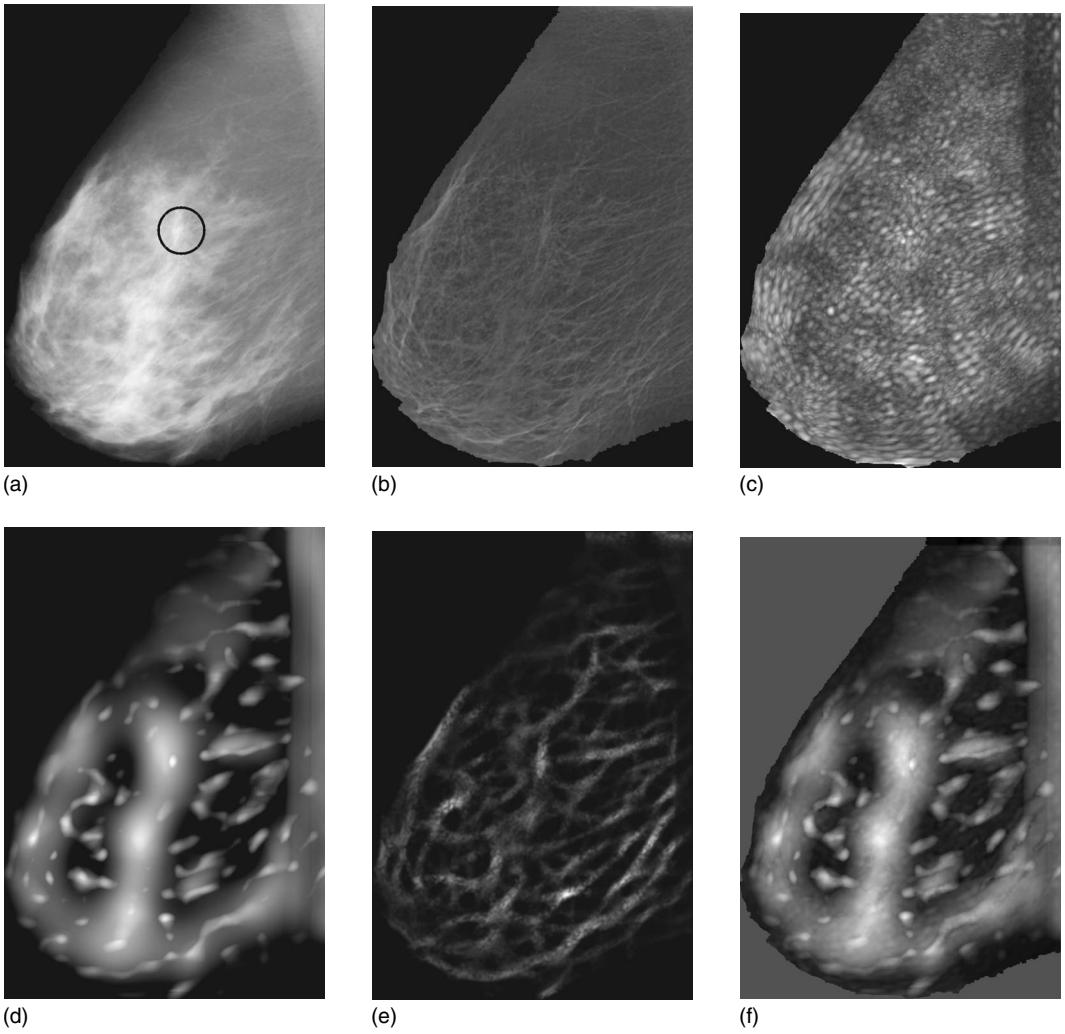

FIG. 10. This figure shows the output obtained at each step of the detection algorithm: (a) Original image and the ground truth outlined by the radiologist. (b) The image obtained from the enhancement algorithm. (c) The output of the spiculated lesion filters (d) The output from the Gaussian filters. (e) The output from oriented DOG filters. (f) The overall output of the detection algorithm.

verge. The SLFs are configured to have sizes, frequencies, and extents derived from actual physical measurements.

IV.D. False positives

In this work, we created models for normal structures that may cause false positives (e.g., oriented difference-of-Gaussian filters to represent blood vessels).

While we do not have complete information about the properties of normal structures, from the measurement studies we know the range of the properties of spicules of spiculated lesions. We note that this strategy to reduce false positives is implemented in parallel with the other components of the detection algorithm, which are geared toward detecting converging spicules and central mass regions. In comparison, in previous approaches the reduction of false positives is carried out sequentially, after the detection of the abnormality. Finally, the motivation for the use of oriented DOG filters (instead of Gabor filters) to extract linear structures is derived from computational models of the human visual system (HVS).[50,51] Numerous studies of the HVS have shown that

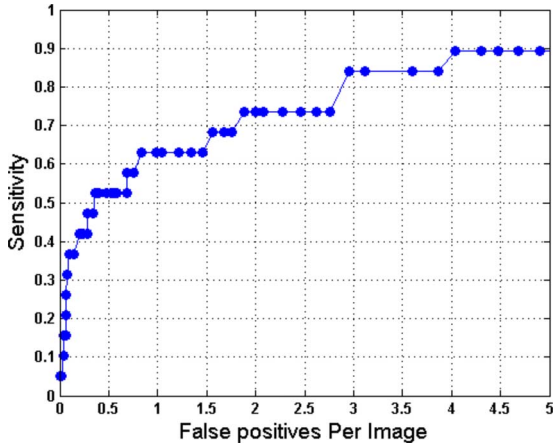

FIG. 11. The performance of the detection algorithm is reported using FROC curves. The *y* axis of the FROC curve corresponds to the sensitivity of the algorithm and the *x* axis corresponds to the number of FPI per image. For the set of 50 images from the MIAS database we achieved a sensitivity of 84% at 3 FPI for the detection of spiculated masses. This set contained all 19 images of spiculated masses from the MIAS database and 31 normal images.

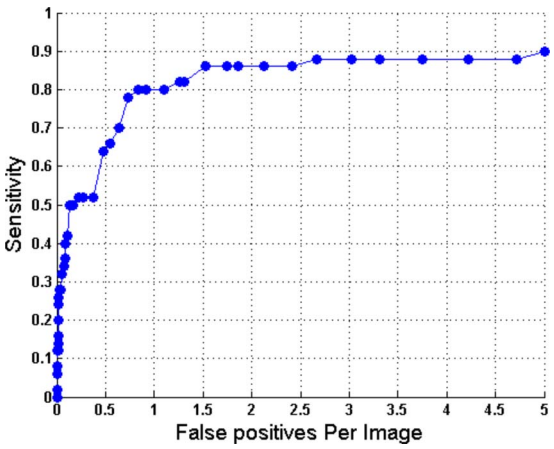

FIG. 12. The performance of the detection algorithm is reported using FROC curves. The *y* axis of the FROC curve corresponds to the sensitivity of the algorithm and the *x* axis corresponds to the number of FPI per image. For the set of 100 images from the DDSM database we achieved a sensitivity of 88% at 2.7 FPI for the detection of spiculated masses. This set contained 50 images of spiculated masses and 50 normal images.

the HVS seems to have adapted DOGs for edge and line handling, whereas Gabor filters appear to be more appropriate for textures and area-based processing. Thus, a number of authors have used Gabor filters for texture segmentation.[37,38,52–57]

IV.E. Detection results and number of false positives

We obtained 84% sensitivity (at 3 FPI) and 88% sensitivity (at 2.7 FPI) for the mini-MIAS and DDSM data sets, respectively. This may seem large compared to other studies on mass detection (e.g., Kegelmeyer *et al.*) Although Kegelmeyer *et al.*[24] reported a very low FP "on their data set," other researchers have not been able to achieve similar results on different data sets.[58,59] The observation that results can vary considerably on different data sets is also seen with commercial CADe systems and it is difficult to get a reliable assessment of the performance of commercially available CADe systems on the detection of masses and spiculated masses. In an early report on the commercial CADe systems, the detection accuracy of microcalcifications was reported as 98.5% sensitivity at 0.74 false positives per case. The detection accuracy of masses was reported as 85.7% at 1.32 false-positive marks per case.[60] In a subsequent study, the CADe system is reported to have a 98.5% sensitivity at 0.185 FPI for microcalcification clusters and a 86% sensitivity at 0.24 FPI for spiculated masses.[18] While the results of the detection of microcalcifications are consistent, the detection results for masses vary considerably. For example, clinical studies to evaluate the performance of commercial CADe systems for mass detection, have reported sensitivities ranging from 67% to 89% with the FPI ranging from 0.40 to 0.74 FPI.[16,17,20–22] For normal images FP rates of 1.3 to 1.8 FPI have been reported.[22,23] It is likely that similar to the case of masses the performance of CADe may vary significantly on the detection of spiculated masses. To the best of our knowledge, only one study has reported the performance of commercial CADe on the detection of spiculated masses.[18] Thus, it is difficult to get a reliable assessment of the performance of commercially available CADe systems on the detection of spiculated masses.

In summary, results of any given CADe algorithm can vary significantly depending on the data set used and two CADe algorithms can only be directly compared when the same training and testing sets are used. The discussion in this article of results of prior studies and commercial systems provides context for our work, but a direct comparison with our results is not meaningful when a different data set was used in the reference study.

IV.F. Detection results reported on images (with all types of masses) from the DDSM

For the detection of masses in the DDSM, Heath *et al.*[61] reported a sensitivity of 80% at 4.5 FPI for the testing set. In another mass detection study, which used images from the DDSM, Catarious *et al.*[62] reported a sensitivity of 80% at 1.6 FPI and a sensitivity of 90% at 4.2 FPI. In a recent article analyzing the effect of DOG parameters, Catarious *et al.*,[63] reported a 81% sensitivity with FPI ranging from 1.35 to 3.66 FPI for different parameter values.[63] It has been reported that the DDSM is a difficult data set. For example, Brake *et al.* obtained a better mass detection performance on the Nijmegen data set (collected in the Netherlands) than on the DDSM data set.[64]

TABLE II. This table summarizes the performance of prior algorithms developed for the detection of spiculated masses. It also presents the number of training and testing images used in each study.

Author	Total No. of images	Total No. of spiculated masses	No. of training images (No. of spiculated masses)	No. of testing images (No. of spiculated masses)	Sensitivity	FPI
Kegelmeyer[a]	330	68	165(34)	165(34)	100	–
Karssemeijer[b]	50	19[e]	14	50(19)[e]	90	1
Delp[c]	38	19	19(9)	19(10)	84.2	1
Zwiggelaar[d]	54	27	(Leave-one-out cross-validation method used)		70	0.01

[a]Reference 21.
[b]Reference 22.
[c]Reference 26.
[d]Reference 28.
[e]In the study by Karssemeijer (Ref. 22), nine spiculated masses and ten architectural distortions were used.

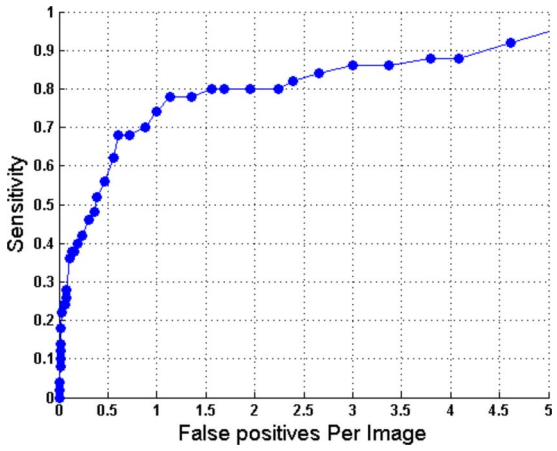

FIG. 13. The FROC curve for a set of 100 images. This set contained 50 images of nonspiculated masses and 50 normal images. A sensitivity of 86% was obtained at 3 FPI. This shows that the algorithm does not generate more false-positives on images of nonspiculated masses.

As our algorithm is designed for the detection of spiculated masses only, it could be applied in sequence with algorithms for detecting other types of lesions. Since our approach is different from other detection methods, it provides complementary information to the overall CADe algorithm. While there is no reason to anticipate that our algorithm will generate more false-positives on images of nonspiculated lesions than on images of normal cases, we present some preliminary results to support this assertion. On a set of 50 images, each containing one nonspiculated mass, we achieved a sensitivity of 86% at 3 FPI (Fig. 13).

IV.G. Advantages and limitations of model-based approach

There are a number of advantages to using a model-based approach. In the future, new knowledge about the properties of structures to be detected can be easily incorporated. Likewise, one can later add in more detailed models of normal structures that lead to false positives (e.g., linear structures in the parenchyma).

The major challenge of a model-based approach is the lack of a straightforward way to decide on the number of candidate "models," i.e., spiculated lesion filters. In this work, the selection of 25 filter banks was an empirical choice and further studies will be required to define an optimal number of filter banks.

Another potential limitation is that the properties of the 25 spiculated lesion filters were selected from measurements from 21 spiculated lesions. In our measurement study, the widths and lengths of all 369 spicules from these 21 spiculated masses were measured. The filter-bank parameters were selected from the joint probability density functions of the properties of the spiculated masses. We believe that once we have a good estimate of the joint probability density function (pdf) of the properties of spiculated masses, we can generate any number of samples (that is filters) from that pdf. The key issue is whether we have obtained a good estimate of the pdf of the properties of the spiculated masses. In future work, we will expand the data set of measurements in order to fine tune our estimate of the pdf.

V. CONCLUDING REMARKS

In this article, we present a new model-based framework for the detection of spiculated masses. We have invented a new class of linear filters, spiculated lesion filters, for the detection of converging lines or spiculations. These filters are highly specific narrowband filters, which are designed to match the expected structures of spiculated masses. As a part of this algorithm, we have also invented a novel technique to enhance spicules on mammograms based on filtering in the radon domain. All parameters of the detection algorithm are set using radiologists' measurements of lesion properties. We have also developed models to reduce the false positives due to normal linear structures.

ACKNOWLEDGMENTS

M.S. was supported the Department of Defense (DoD) Congressionally Directed Medical Research Program (CDMRP) predoctoral fellowship W81XWH-04-1-0406. We thank the U.T. Center for Biomedical Engineering for seed grant funding. This work was also supported in part by an Early Career Award from the Wallace H. Coulter Foundation. We would like to thank Dr. Reyer Zwiggelaar for reading the manuscript and providing valuable feedback. Finally, we appreciate the technical support in the BMIL provided by Chris Kite, Zack Mahdavi, and Scott Swanson.

[a]Portions of this study related to the detection algorithm were presented at SPIE Medical Imaging conference in San Diego in February 2005. Portions of the measurement studies were presented at the Medical Image Perception Conference XI held at Windermere, UK in September 2005.

[b]Author to whom correspondence should be addressed. Telephone: +1.512.471.1711; Fax: +1.512.471.0616. Electronic mail: mia.markey@mail.utexas.edu

[1]American Cancer Society, "Cancer facts and figures 2007," 2007.
[2]E. J. Feuer *et al.*, "The lifetime risk of developing breast cancer," J. Natl. Cancer Inst. **85**, 892–897 (1993).
[3]L. M. Wun, R. M. Merrill, and E. J. Feuer, "Estimating lifetime and lge-conditional probabilities of developing cancer," Lifetime Data Anal. **4**, 169–186 (1998).
[4]American College of Radiology, *ACR BI-RADS—Mammography, Ultrasound & Magnetic Resonance Imaging*, 4th ed. (American College of Radiology, Reston, VA, 2003).
[5]L. Liberman *et al.*, "The breast imaging reporting and data system: Positive predictive value of mammographic features and final assessment categories," AJR Am. J. Roentgenol. **171**, 35–40 (1998).
[6]C. H. Lee, "Screening mammography: Proven benefit, continued controversy," Radiol. Clin. North Am. **40**, 395–407 (2002).
[7]K. Kerlikowske *et al.*, "Performance of screening mammography among women with and without a first-degree relative with breast cancer," Ann. Intern. Med. **133**, 855–863 (2000).
[8]T. M. Kolb, J. Lichy, and J. H. Newhouse, "Comparison of the performance of screening mammography, physical examination, and breast US and evaluation of factors that influence them: An analysis of 27,825 patient evaluations," Radiology **225**(1), 165–175 (2002).
[9]R. E. Bird, T. W. Wallace, and B. C. Yankaskas, "Analysis of cancers missed at screening mammography," Radiology **184**, 613–617 (1992).
[10]M. L. Giger, "Computer-aided diagnosis in radiology," Acad. Radiol. **9**, 1–3 (2002).
[11]M. L. Giger, N. Karssemeijer, and S. G. Armato III, "Computer-aided diagnosis in medical imaging," IEEE Trans. Med. Imaging **20**, 1205–1208

(2001).
[12]M. L. Giger, "Computer-aided diagnosis of breast lesions in medical images," Comput. Sci. Eng. **2**, 39–45 (2000).
[13]K. Doi *et al.*, "Computer-aided diagnosis in radiology: Potential and pitfalls," Eur. J. Radiol. **31**, 97–109 (1999).
[14]C. J. Vyborny, M. L. Giger, and R. M. Nishikawa, "Computer-aided detection and diagnosis of breast cancer," Radiol. Clin. North Am. **38**, 725–740 (2000).
[15]M. P. Sampat, M. K. Markey, and A. C. Bovik, "Computer-aided detection and diagnosis in mammography," in *Handbook of Image and Video Processing*, edited by A. C. Bovik (Academic, New York, 2005), p. 1195–1217.
[16]L. J. W. Burhenne *et al.*, "Potential contribution of computer-aided detection to the sensitivity of screening mammography," Radiology **215**, 554–562 (2000).
[17]T. W. Freer and M. J. Ulissey, "Screening mammography with computer-aided detection: Prospective study of 12,860 patients in a community breast center," Radiology **220**, 781–786 (2001).
[18]C. J. Vyborny *et al.*, "Breast cancer: Importance of spiculation in computer-aided detection," Radiology **215**, 703–707 (2000).
[19]D. Gur *et al.*, "Changes in breast cancer detection and mammography recall rates after the introduction of a computer-aided detection system," J. Natl. Cancer Inst. **96**(3), 185–190 (2004).
[20]M. Bazzocchi *et al.*, "CAD systems for mammography: A real opportunity? A review of the literature," Radiol. Med. (Torino) **112**, 329–353 (2007).
[21]R. L. Birdwell *et al.*, "Mammographic characteristics of 115 missed cancers later detected with screening mammography and the potential utility of computer-aided detection," Radiology **219**, 192–202 (2001).
[22]S. K. Yang *et al.*, "Screening mammography-detected cancers: Sensitivity of a computer-aided detection system applied to full-field digital mammograms," Radiology **244**, 104–111 (2007).
[23]R. F. Brem *et al.*, "Evaluation of breast cancer with a computer-aided detection system by mammographic appearance and histopathology," Cancer **104**, 931–935 (2005).
[24]W. P. Kegelmeyer, Jr. *et al.*, "Computer-aided mammographic screening for spiculated lesions," Radiology **191**, 331–337 (1994).
[25]N. Karssemeijer and G. M. te Brake, "Detection of stellate distortions in mammograms," IEEE Trans. Med. Imaging **15**, 611–619 (1996).
[26]L. Sheng, C. F. Babbs, and E. J. Delp, "Multiresolution detection of spiculated lesions in digital mammograms," IEEE Trans. Image Process. **10**, 874–884 (2001).
[27]M. Zhang *et al.*, "Mammographic texture analysis for the detection of spiculated lesions," proc. IWDM, **1119**, 347–350 (1996).
[28]R. Zwiggelaar *et al.*, "Model-based detection of spiculated lesions in mammograms," Med. Image Anal. **3**, 39–62 (1999).
[29]M. P. Sampat *et al.*, "The reliability of measuring physical characteristics of spiculated masses on mammography," Br. J. Radiol. **79**, S134–S140 (2006).
[30]A. Bovik, *Handbook of Image & Video Processing*, 2nd ed. (Academic, New York, 2005).
[31]A. Papoulis, *The Fourier Integral and Its Applications* (McGraw-Hill, New York, 1962).
[32]A. Kak and M. Slaney, *Principles of Computerized Tomographic Imaging* (IEEE, New York, 1998).
[33]A. Averbuch *et al.*, "Fast slant stack: A notion of radon transform for data in a Cartesian grid which is rapidly computable, algebraically exact, geometrically faithful and invertible," Technical Report, Stanford University, 2001, available online at http://www-stat.stanford.edu/~donoho/Reports/2001/FastSlantStack.pdf.
[34]M. P. Sampat *et al.*, "Comparison of algorithms to enhance spicules on spiculated lesions on mammography," J. Digit. Imaging **21**(1), 9–17 (2008).
[35]M. P. Sampat and A. C. Bovik, "Detection of spiculated lesions in mammograms," Proc. IEEE-EMBS **1**, 810–813 (2003).
[36]M. P. Sampat *et al.*, "Evidence-based detection of spiculated masses and architectural distortions," Proc. SPIE **5747**, 26–37 (2005).
[37]A. C. Bovik, M. Clark, and W. S. Geisler, "Multichannel texture analysis using localized spatial filters," IEEE Trans. Pattern Anal. Mach. Intell. **12**, 55–73 (1990).
[38]A. C. Bovik, "Analysis of multichannel narrow-band filters for image texture segmentation," IEEE Trans. Signal Process. **39**, 2025–2043 (1991).
[39]A. C. Bovik *et al.*, "Localized measurement of emergent image frequencies by Gabor wavelets," IEEE Trans. Inf. Theory **38**, 691–712 (1992).
[40]M. Heath *et al.*, "The digital database for screening mammography," Proc. IWDM 212–218 (2000).
[41]http://marathon.csee.usf.edu/Mammography/Database.html.
[42]J. Suckling *et al.*, "The mammographic images analysis society digital mammogram database," Exerpta Medica **1069**, 375–378 (1994).
[43]http://peipa.essex.ac.uk/info/mias.html.
[44]http://bmil.bme.utexas.edu/.
[45]http://rsb.info.nih.gov/ij/.
[46]C. Yang *et al.*, "Improved fast gauss transform and efficient kernel density estimation," Proc. IEEE ICCV **1**, 464–471 (2003).
[47]C. Varela *et al.*, "Use of prior mammograms in the classification of benign and malignant masses," Eur. J. Radiol. **56**, 248–255 (2005).
[48]R. Saunders *et al.*, "Simulation of mammographic lesions," Acad. Radiol. **13**, 860–870 (2006).
[49]R. Zwiggelaar *et al.*, "Linear structures in mammographic images: Detection and classification," IEEE Trans. Med. Imaging **23**, 1077–1086 (2004).
[50]D. Marr, *Vision: A Computational Investigation into the Human Representation and Processing of Visual Information* (W. H. Freeman, San Francisco, CA, 1982).
[51]L. Cormack, *Computational Models of Early Human Vision*, edited by A. C. Bovik (Academic, New York, 2005).
[52]D. Dunn and W. E. Higgins, "Optimal Gabor filters for texture segmentation," IEEE Trans. Image Process. **4**, 947–964 (1995).
[53]A. Teuner, O. Pichler, and B. J. Hosticka, "Unsupervised texture segmentation of images using tuned matched Gabor filters," IEEE Trans. Image Process. **4**, 863–870 (1995).
[54]G. M. Haley and B. S. Manjunath, "Rotation-invariant texture classification using a complete space-frequency model," IEEE Trans. Image Process. **8**, 255–269 (1999).
[55]M. Clark, A. Bovik, and S. Geisler, "Texture segmentation using Gabor modulation and demodulation," Pattern Recogn. Lett. **6**, 261–267 (1987).
[56]A. K. Jain and F. Farrokhnia, "Unsupervised texture segmentation using Gabor filters," Pattern Recogn. **24**, 1167–1186 (1991).
[57]T. P. Weldon, W. E. Higgins, and D. F. Dunn, "Efficient Gabor filter design for texture segmentation," Pattern Recogn. **29**, 2005–2015 (1996).
[58]G. M. te Brake, N. Karssemeijer, and J. H. Hendriks, "Automated detection of breast carcinomas not detected in a screening program," Radiology **207**, 465–471 (1998).
[59]K. Woods and K. W. Bowyer, "A general view of detection algorithms," Proc. IWDM **1119**, 385–390 (1996).
[60]U.S. Food and Drug Administration, "Summary of safety and effectiveness data: R2 technologies (P970058)," 1998.
[61]M. D. Heath and K. W. Bowyer, "Mass detection by relative image intensity," Proc. IWDM 219–225 (2000).
[62]D. M. Catarious, Jr., A. H. Baydush, and C. E. Floyd, Jr., "Incorporation of an iterative, linear segmentation routine into a mammographic mass CAD system," Med. Phys. **31**, 1512–1520 (2004).
[63]D. M. Catarious, Jr., A. H. Baydush, and C. E. Floyd, Jr., "Characterization of difference of Gaussian filters in the detection of mammographic regions," Med. Phys. **33**, 4104–4114 (2006).
[64]G. M. te Brake, N. Karssemeijer, and J. H. Hendriks, "An automatic method to discriminate malignant masses from normal tissue in digital mammograms," Phys. Med. Biol. **45**, 2843–2857 (2000).